Crossflow instabilities under plasma actuation

Design, commissioning and preliminary results of a new experimental facility

Peng, K.; Avallone, F.; Kotsonis, M.

Important note
To cite this publication, please use the final published version (if applicable).
Please check the document version above.

Crossflow instabilities under plasma actuation: Design, commissioning and preliminary results of a new experimental facility

K. Peng[*], F. Avallone[†] and M. Kotsonis[‡]
Delft University of Technology, Delft, The Netherlands, 2629HS

Plasma-based flow control poses a simple and robust technique for transition delay on swept wings. However, a clear understanding of how plasma actuators affect crossflow instabilities is necessary to develop and mature crossflow control based on plasma actuators. In this paper, the design of a new swept wing model optimised for the study of crossflow receptivity and stability under plasma actuator is described in detail. First, a 2D wing shape is designed, to match the nearing leading edge pressure distribution of a reference high-Reynolds number swept wing model (*M3J*) which has been used extensively in past investigations. The aerodynamic performance of this new shape is investigated using CFD simulations and the results show a good agreement for the pressure coefficient. In manufacturing design, the wing model features provisions to accept plasma actuators, such as non-conductive material as well as an appropriately designed recess for the actuator assembly. The new model in conjunction with a recently refurbished low turbulence windtunnel facility are characterized in a preliminary experiment. The uniformity and quality of the flow is identified using pressure measurements and the results confirm the new model achieved near-invariant spanwise conditions until 40% of the chord. Infrared thermography is used to capture the surface footprint of stationary primary crossflow vortices. Clear formations of stationary vortices created by discrete roughness are captured and no visible transition is observed. Finally, the effects of plasma actuation on crossflow instabilities are inspected by Infrared Thermography and PIV scanning. The results validate the prediction of Linear Stability Theory with respect to the most unstable stationary mode and traveling mode. The appearance of secondary crossflow instabilities is observed at relatively upstream chord locations even without transition detected. The outcome positively confirms the ability of this new model to reproduce receptivity and initial growth of crossflow instabilities of the reference model (*M3J*) under plasma actuation.

Nomenclature

X,Y,Z	=	Global coordinate system parallel to the wind tunnel floor
x,y,z	=	Local coordinate system orthogonal to the wing leading edge
U_∞	=	Freestream velocity along the axis X
U	=	Freestream velocity component along the axis x
W	=	Freestream velocity component along the axis z
u	=	Velocity component along the axis x

---

[*] PhD Candidate, Section of Aerodynamics, Faculty of Aerospace Engineering.
[†] Assitant Professor, Section of Aeroacoustics, Faculty of Aerospace Engineering.
[‡] Associate Professor, Section of Aerodynamics, Faculty of Aerospace Engineering.

w	=	Velocity component along the axis z
c_X	=	Wing chord length in X direction
c_x	=	Wing chord length in x direction
C_p	=	Pressure coefficient
α	=	Angle of attack
d	=	Diameter of discrete roughness element
h	=	Height of discrete roughness element
Re_X	=	Reynolds number based on c_X
Re_x	=	Reynolds number based on c_x
λ	=	Spanwise-wavelength of crossflow instability
f	=	Frequency of crossflow instability
f_{AC}	=	Actuation frequency of plasma actuator
PIV	=	Particle Image Velocimetry
LST	=	Linear Stability Theory

I. Introduction

In the design of modern aircraft, wings are usually placed at a sweep angle which creates a crossflow (CF) within the boundary layer perpendicular to the external streamline direction. This CF component introduces the so-called crossflow instabilities (CFI) into the boundary layer, eventually leading to transition and the associated increase of skin friction [1]. A wide range of techniques have been studied and developed to control the CFI, including Hybrid Laminar Flow Control (HLFC), Discrete Roughness Elements (DRE) and so on [2]. However, these methods have their own disadvantages. Usually, HLFC is associated to increased complexity and cost while DRE are sensitive to wing surface roughness. Compared with these conventional methods, plasma actuator (PA) is a new promising technique as it has low power consumption, fast response, and fully electronic operation with no moving parts [3]. In recent times, efforts have been made both in simulation and experiment to investigate PA's effects on CFI. Kloker et al [4-7] use plasma/DRE simulation to investigate PA effects on CFI following the upstream flow deformation (UFD), base-flow manipulation (BFM) and direct attenuation concepts. Their promising simulation results based on these concepts indeed demonstrate PA has a strong ability for controlling CFI. In recent experiments, Serpieri et al [7] and Yadala et al [8] succeed in using PAs to achieve CFI control based on UFD and BFM respectively.
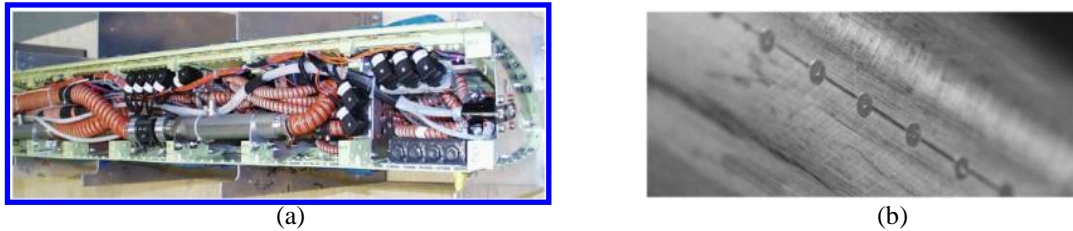

Fig. 1 CF control techniques. (a) Leading edge of the Do 228 test aircraft equipped for HLFC flight test [9]. (b) DRE installed near the leading edge [7].

Notwithstanding the preliminary success of PAs in controlling crossflow transition, a major challenge in the maturing of such approaches remains in the inherently unsteady nature of plasma-based forcing. Moreover, one of the most pertinent questions remaining in the field of PA control on CF is the receptivity of the latter where small changes of initial conditions can lead to distinct boundary layer development and transition. As such, increased effort towards understanding the receptivity and development of CFI to unsteady input, inherent to PA is necessary. Towards this goal, a new swept wing model specifically for PA experiments on CFI is designed and deployed in the Anechoic Vertical Tunnel (AVT) at Delft University of Technology.

This paper presents a description of the design and manufacturing of a new wing model followed by preliminary experimental results. First, the new wing geometry is modified based on the reference wing model (*M3J*). The aerodynamic performance of this new shape is validated by CFD simulations. The calculation gives a good pressure matching with the target C_p and no separation is observed at the pressure side. Then the new swept wing is designed in CAD model and manufactured specifically for PA experiment. Finally, a preliminary experiment aimed at demonstrating the new model's performance was conducted in AVT in Delft University of Technology. To assess the new model's aerodynamic features and the PA controlling effects on its boundary layer, several measurements have been done. First, the pressure is recorded at several angles of attack (*AOA*) to compare with the target C_p and to choose

the desired *AOA* for following measurements. Pressure results are then used as the input for Linear Stability Theory (LST) code to calculate *N*-factors and predict the stability properties of stationary and traveling mods. Finally, Infrared thermography and PIV are used to visualize CF vortex topology and PA effects on CFI. Final experimental results validate the ability of this new swept wing model to study PA effects on the receptivity and initial growth of CFI.

II.   Model Design

A. 2D Wing Shape Design

To design the new wing model, the frequently used swept wing model *66018M3J* (*M3J*) designed at TU Delft is chosen as a reference. This reference model features a uniform spanwise pressure distribution when placed at mild angles of attack which guarantees the infinite swept wing condition. A small leading radius and a favorable pressure gradient until $x/c_x \approx 0.65$ on the pressure side contribute to a boundary layer dominated by crossflow instabilities. More information and details about this model can be found in [10]. Considering CF development is mainly controlled by the favorable pressure gradient along the chord, the CFI growth could be reproduced if the new model's C_p resembles that of the *M3J*. Starting from this consideration, a 2D wing cross section is designed first by the pressure inverse calculation of *XFLR5* with the *M3J* prototype and finer adjustments are further done by *Xfoil*. It should be noted here both the new shape and the *M3J* are calculated by *Xfoil* thus no windtunnel wall effect is considered here. The ultimate comparisons of C_p and geometry (dimensional) between the two wing shapes are shown in fig.2.
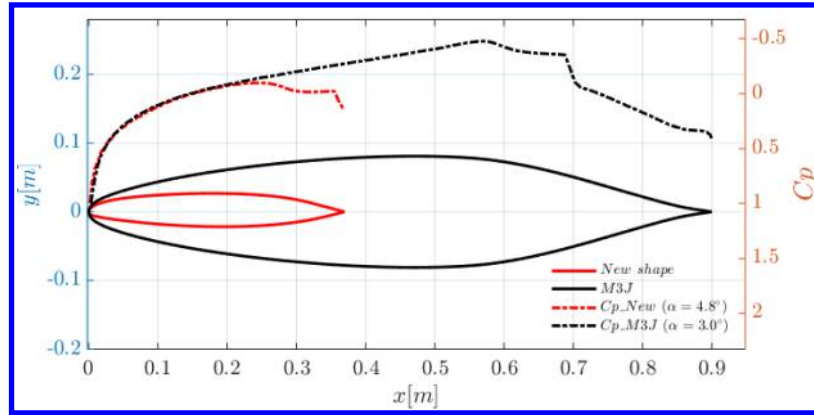

Fig. 2 Two-dimensional geometry and pressure coefficient of the new shape and the *M3J*

Compared with the *M3J*, this new shape is much flatter and thinner in geometry, featuring an even smaller curvature radius at the leading edge. All these facts give the condition for a favorable C_p formation as well as a delayed adverse pressure gradient point [11]. In the current design, the 2D wing shape is in unswept direction (in *x-y* plane) and only the flow component in *x* direction (*u*) is considered in calculation. It should be noted that the C_p used here as a reference is the pressure distribution on the *M3J* that starts from the stagnation point until $x/c_x \approx 0.3$ (pressure side) with an angle of attack $\alpha = 3°$. In this case, a freestream velocity $U_\infty = 25m/s$ is chosen, corresponding to $U=17.7m/s$ (*x* component). Reynolds numbers Re_x for the *M3J* and the new shape are 1.53×10^6 and 4.03×10^5 respectively. A close agreement of C_p between the new shape ($\alpha = 4.8°$) and the *M3J* ($\alpha = 3.0°$) is observed, as displayed in fig.2.

B. CFD Simulation and CAD design

In this section, the aerodynamic performance of this new wing shape is validated by CFD simulation. The widely used two-equation RANS *k-ε* turbulence model is solved by the commercial software *Comsol*. In the calculation of *Xfoil*, the windtunnel wall effect is not taken into consideration thus eliminating the blockage influence. However, in the actual test section for the experiment, the blockage created by walls will accelerate the surrounding flow thus decreasing the pressure. In order to simulate the real condition, the calculation domain is set as similar to the test section dimension as shown in fig.3 (a). In this simulation, the calculation is only implemented in unswept direction (*x*) as the wing model is assumed to be infinite in spanwise direction (*z*). As a result, the *x* component of freestream velocity is given as $U=17.7m/s$ and the wall condition is set as no-slip.
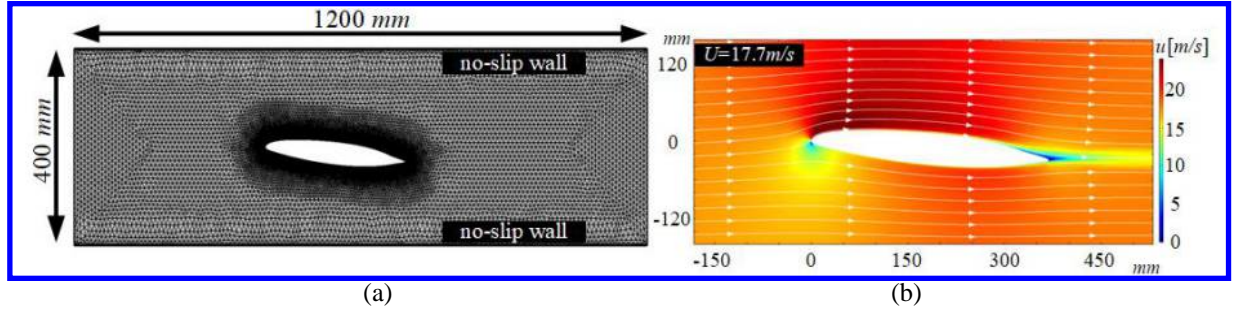
Fig. 3 (a) The calculation domain and mesh of the CFD simulation.
(b) The average velocity field (u) with selected streamlines (white arrows).

As presented in fig.4, a good agreement between the new shape's C_p (light blue) and the target C_p (black) is achieved. Different from the target C_p in the previous section, the one used here is the experimental C_p of the *M3J* (α=3.0°). The simulation outcome verifies that the new shape is still capable to reproduce the initial pressure distribution of the *M3J* considering the windtunnel wall effects. In addition, the flow separation which indicates the laminar extension of the boundary layer as well as the boundary layer stabilization is inspected as well. The average-velocity field of u (with streamlines of white arrows) is illustrated in fig.3(b). As expected, at the chosen *AOA* (α=4.75°), no separation is observed at the pressure side and only a small separation is visible on the suction side near the trailing edge, which guarantees an extensive laminar flow region on the pressure side.
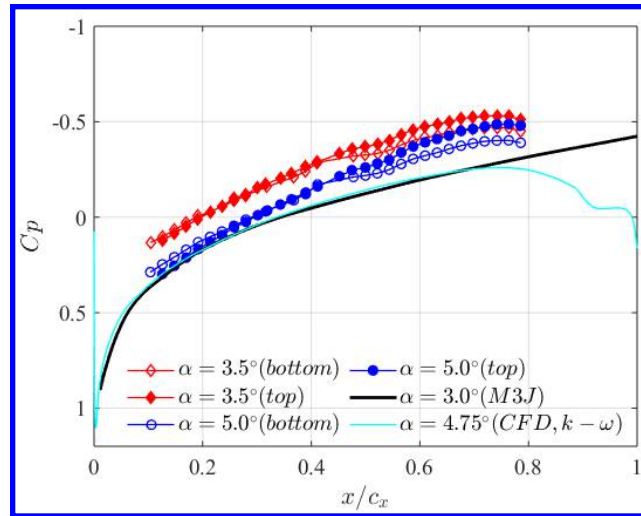

Fig. 4 The pressure coefficient of simulation (light blue line),
experiment (red and blue marks) and the target (black line)

Based on the satisfactory outcomes from CFD simulation, the 2D new shape is chosen as the prototype to design and manufacture the CAD swept wing model. The wing model has a sweep angle of 45° and a dimension of 980mm ×370mm as shown in fig.5(b). Recalling this model is specifically designed for PA study, there are two requirements that should be put into consideration. First is that PA is fully electrical which means the material of the wing model should be non-metallic and insulated to avoid any electrical interference. In addition, as the wing model needs to be separated into 2 parts for the purpose of pressure tap and shaft installation, the bending deformation of plastic material during manufacture should be taken into consideration. Based on these considerations, the new model is designed to be a composition of two individual pieces, with the measuring part made of Polyoxymethylene (POM) and the back part made of aluminum. In addition, a broad groove with a depth of 3.1mm is designed for the installation of the PA and dielectric materials. The dimension of the groove is designed to be approximately 1/3 of the model's total spanwise length and extend to $x/c_x \approx 0.8$. In addition, two white dash stripes in fig.5(b) represent positions of pressure tap arrays. Due to manufacturing difficulties caused by the extremely small radius of the leading edge, the pressure tap array is not including taps at the leading edge and surrounding field (in other words, the array spans from $x/c_x \approx 0.1$ to 0.8). With respect to the test section, it's closed by four walls of transparent plastic. The ending exit of the test section is

4

designed to follow the wing trailing edge for the convenience to install subsequent measuring system (e.g. the hot-wire measuring system). The ultimate CAD model is shown in fig.5.
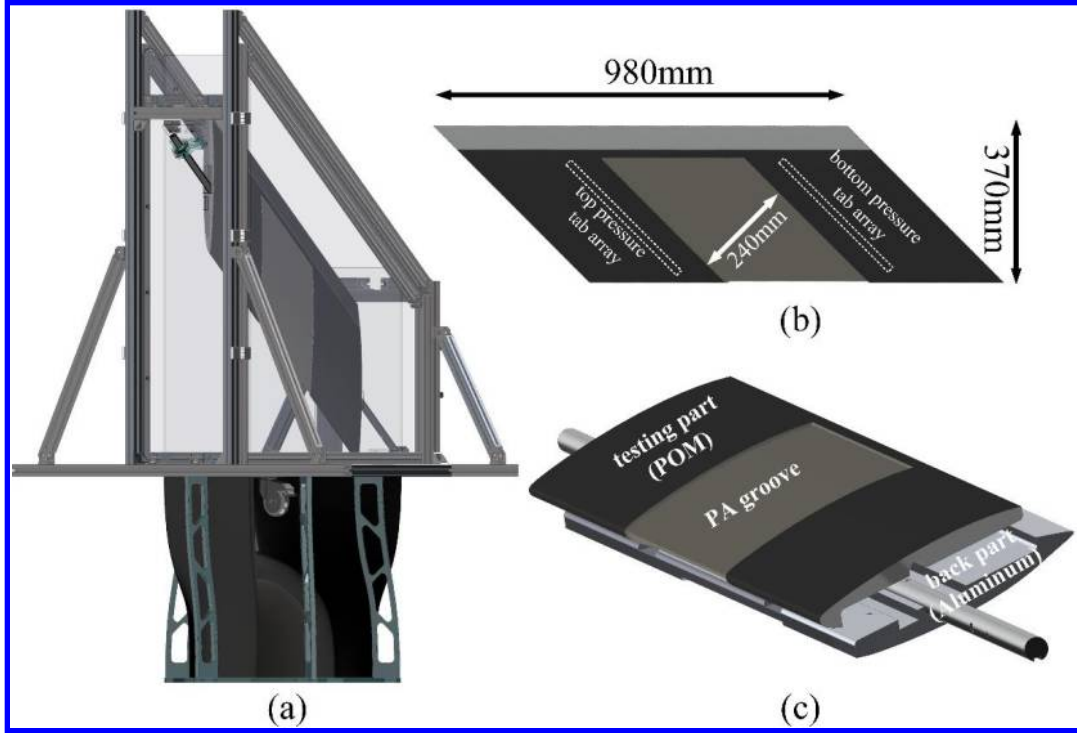

Fig. 5 (a) CAD model of the test section installed on the contraction. (b) The top view of the wing model. (c) CAD model of the assembly of testing part, shaft and back part.

III. Experimental set-up and measurement techniques

A. Wing Model and Windtunnel Facility

The current experiment aimed at verifying the new model's performance is conducted in the open-jet, anechoic wind tunnel at TU Delft Low Speed Lab [12]. The test section used is $400mm \times 700mm$ in cross-section and features a low turbulence environment (turbulence intensity less than 0.04%). In this paper, two reference systems are defined as one for windtunnel (denoted as *XYZ*) and the other one associated with the swept wing model (*xyz*). In addition, *Y* coincides with *y* and is perpendicular to the wing surface. The schematic of these two coordinate systems is illustrated in fig.6(b). In order to avoid flow separation at the adverse pressure gradient region, zig-zag tapes are used to trigger the boundary layers at the pressure side ($x/c_x \approx 0.8$) and the suction side ($x/c_x \approx 0.2$). All measurements in this experiment are conducted at the freestream velocity of $U_\infty = 22m/s$ (corresponding to Reynolds number Re_X of 7.6×10^5) with the wing model at the fixed *AOA* ($\alpha = 3.5°$).

B. Plasma Actuator

The groove designed for PA is filled with a composite layer of PET foils of different thickness on which the plasma actuator is placed. The PA used in the current experiment is uniform in the spanwise direction and positioned at $x/c_x = 0.08$, parallelling to the leading edge. Both ground and exposed electrodes are fabricated with conductive silver paint with a dimension of $355mm \times 5mm$. Specifically, there is no gap or overlap between electrodes and the ground electrode is located more upstream. Thus the wall jet created by the PA will be directed against the freestream. The dielectric layer is made of a composite of PET foils with a total thickness of $500\mu m$. To avoid any step on the surface, the PET foil as dielectric material is extended to wrap around the leading edge, as illustrated in fig.6(c).
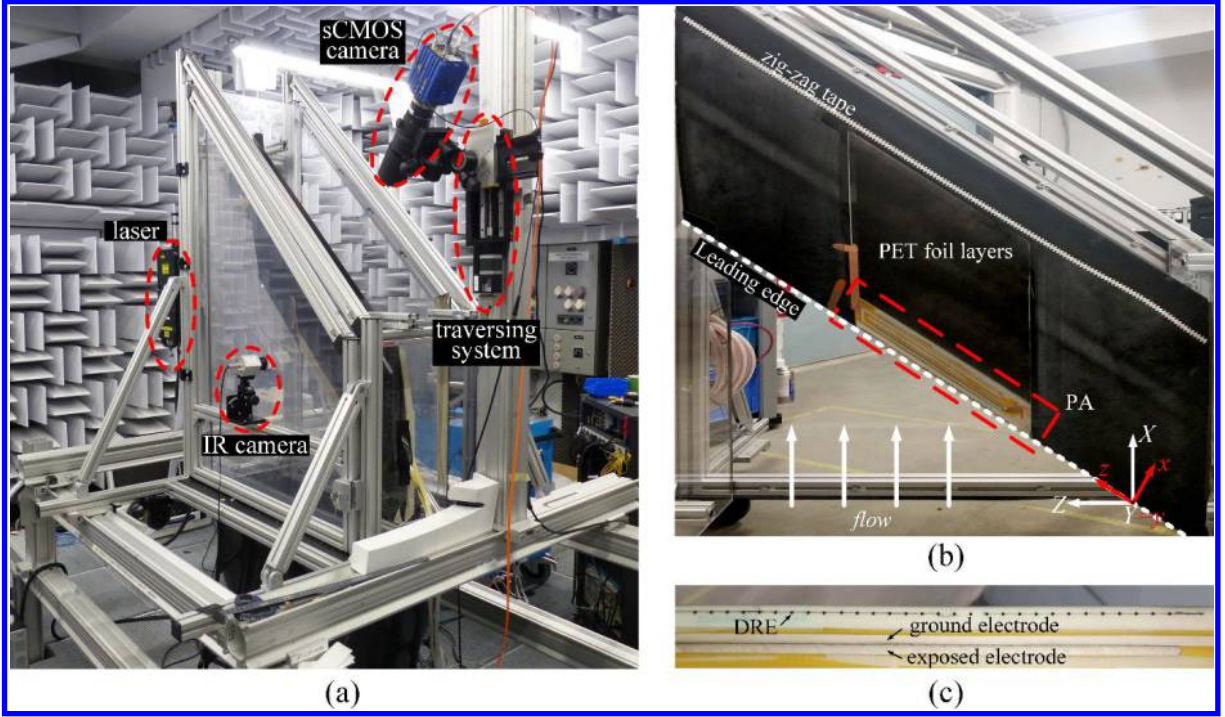
Fig. 6 (a) The experimental test section installed on the contraction (in AVT). (b) Top view of the real model and two reference systems. (c)The plasma actuator and DRE

It should be noted here, the AC signals used for the PA are different in thermography and PIV measurements as illustrated in fig.7. AC signals in IR section apply the same duty cycle of 50% with a carrier frequency of $5000Hz$. However, in PIV section, the carrier frequency is $4000Hz$ and the duty cycle is modulated in the way that every individual pulse sequence features an equal width ($1.2ms$) thus having similar power. Specifically, the duty cycle of AC signals is adjusted to be 12%, 24%, 36%, 48% and 96% corresponding to f_{AC}=100Hz, 200Hz, 300Hz, 500Hz and 800Hz.
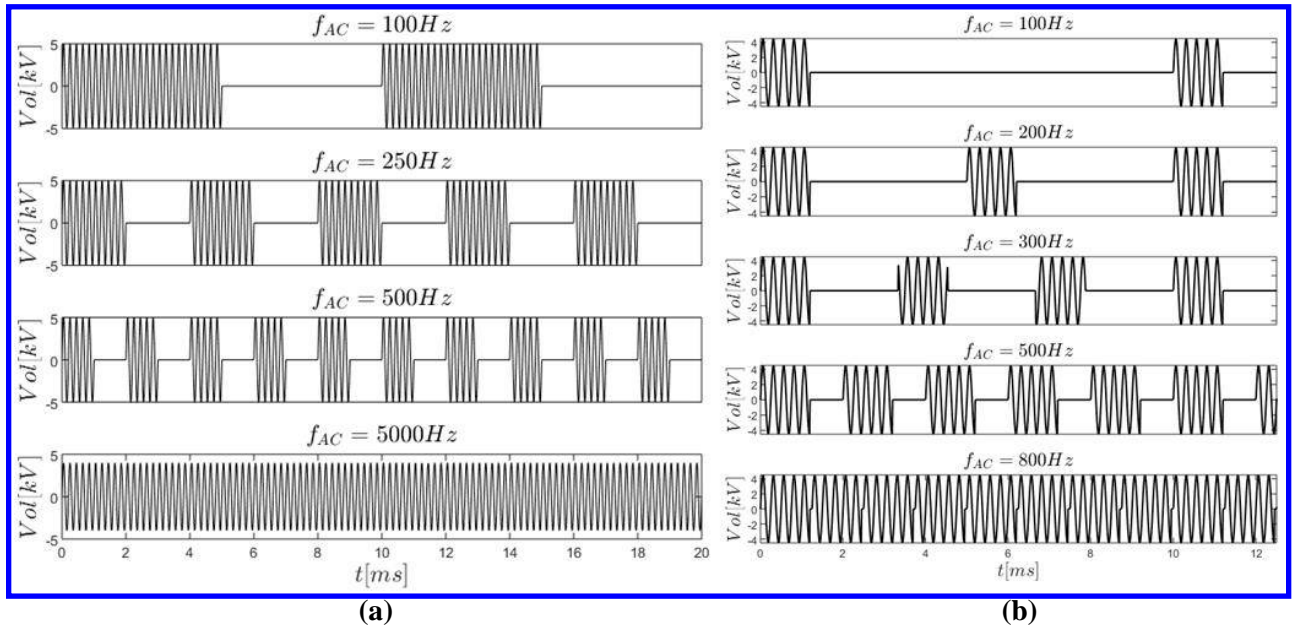

Fig. 7 AC signals of the plasma actuator in (a) IR measurement (b) PIV measurement

C. Infrared Thermography

An Optris PI640 IR camera is used to record surface temperature through a small opening in the test section vertical wall as shown in fig.6(a). The IR camera has a thermal sensitivity of $75mK$ and captures IR images at a rate of $4Hz$. Approximately 50 images are collected for each case and are averaged to improve the signal to noise ratio. In order to improve the contrast between low and high shear flow regions (namely the laminar and turbulent regions), two halogen lamps ($500W$ each) are used to irradiate the wing surface. In the current experiment, as only the flow topology features are of interest, no temperature calibration is performed.

D. Planar Particle Image Velocimetry (PIV)

Planar PIV scanning is performed in y-z planes along the streamwise direction (from x/c_x =0.1 to 0.35). The laser source used is a Quantel Evergreen Nd: YAG dual cavity laser ($200mJ$ pulse energy and λ=$532nm$ wavelength). The beam is properly manipulated by optics and shaped in a sheet of approximately $1mm$ thickness. A LaVision Imager sCMOS camera (sCMOS, 2560×2160 pixels, 16-bit, $6.5\mu m$ pixel pitch) is coupled with a Nikon Micro-Nikkor objective featuring a focal length of $200mm$. The aperture is set to $f_\# = 8$ and the magnification factor is $54.2px/mm$, giving a view window of $47.7mm \times 40.4mm$. The laser and camera are shifted together by a traversing system which allows to maintain their alignment and focus during scanning. For each chord location, 2000 image pairs are acquired at a frequency of $14.9Hz$.

IV. Experimental results

A. Pressure Distribution

In the current experiment, the new model's pressure distribution is measured under α=3.5° and α=5° respectively. The results are displayed in fig.4 along with the reference C_p (*M3J*, α=3°). The 'bottom' and 'top' marks in the legend indicate positions of the pressure tap arrays (also illustrated in fig.5). The bottom array is located at the wing side which is closer to the coming flow (i.e. the contraction inlet). As mentioned in previous sections, the new model is designed to replicate the initial C_p (i.e. near the leading edge) of the *M3J* and validated in CFD simulation. However, a distinct discrepancy is observed between the experimental C_p and the simulation though the former indeed follows the latter's curve. In addition, it can be noticed that the experimental C_p is lower in amplitude than the simulated one, suggesting a strong blockage effect appears in the current experiment. Compared with the 2D simulation model, a significant difference in experiment is that the test section is not fully closed since the open-jet windtunnel is used. In addition, the experimental test section is not long enough as it only covers until the trailing edge. These facts result in a considerable wake effect immediately at the trailing edge thus deviating the pressure distribution. In addition, it's also observed in both experimental cases, the top pressure tap array initially matches well with the bottom array and then grows remarkably lower than the latter after x/c_x=0.4. This observed discrepancy that happens downstream also demonstrates the wake effects introduced in the current experiment. Furthermore, the blockage created in the test section as well contributes to the observation: the top tap array is placed more downstream in the wind tunnel than the bottom one thus resulting in experiencing an already enhanced blockage caused by the bottom part of the wing. Despite the C_p discrepancy indicating a non-uniformity along span-wise direction after x/c_x=0.4, this result is an integrated effect over a long distance of $424.26mm$ (i.e. the span-wise distance between the bottom and the top pressure tap arrays). Therefore, a zoomed measuring region at the mid-span only including several stationary vortices can significantly reduce the non-uniformity and hence could be regarded as invariant in spanwise. Moreover, the smooth slope of pressure distribution and the correspondence of experimental C_p curves with the reference still suggest that initial and linear CFI growth from the new model can be expected to be similar to the *M3J*'s. As a conclusion, the experiment results manifest that this new model features the ability to serve as a model for receptivity and initial growth study of CFI.

B. Linear Stability Theory (LST)

In a swept wing boundary layer, the CFI is generally characterized by traveling modes and stationary modes. These instability modes have various frequencies and wavelengths and hence feature different spatial amplification rates. Among these instabilities, the stationary mode is usually responsible for transition in most of low-turbulence experiments and flights because of its higher initial amplitude and low turbulence intensity in the environment [13]. On the other hand, a PA is inherently introducing a range of unsteady perturbations thus able to trigger several traveling modes [14]. Therefore, a stability property estimation for both stationary and traveling modes over the new model is required to help design the experiment. One of the available tools is Linear Stability Theory (LST) which has been

extensively used in past experiments to predict the stability properties [15] with respect to various wavelength λ as well as frequency f.

In this paper, the measured pressure distribution from the experiment is used to calculate the laminar boundary layer solution first and then to solve the Orr-Sommerfeld (O-S) equation. As a result, the stability diagrams of N-factor which indicates the integration of growth rates (α_i) along x are shown in fig.8 for f=0Hz (stationary mode), 300Hz and 500Hz modes respectively. It's evident that stationary modes with λ=7mm to 8mm obtain the highest N-factors under the current experiment condition. This fact once again demonstrates the similarity of CFI growth on the new model with that on the $M3J$ (where the λ=8mm stationary mode dominates the boundary layer stability[8]). As a result, the λ=8mm stationary mode is chosen in the current experiment as the DRE spacing. Furthermore, according to fig.8, frequency has a remarkable effect on disturbance amplification. Compared with the 0Hz case, modes with 300Hz grow stronger and faster along x while modes with 500Hz start to decrease significantly.
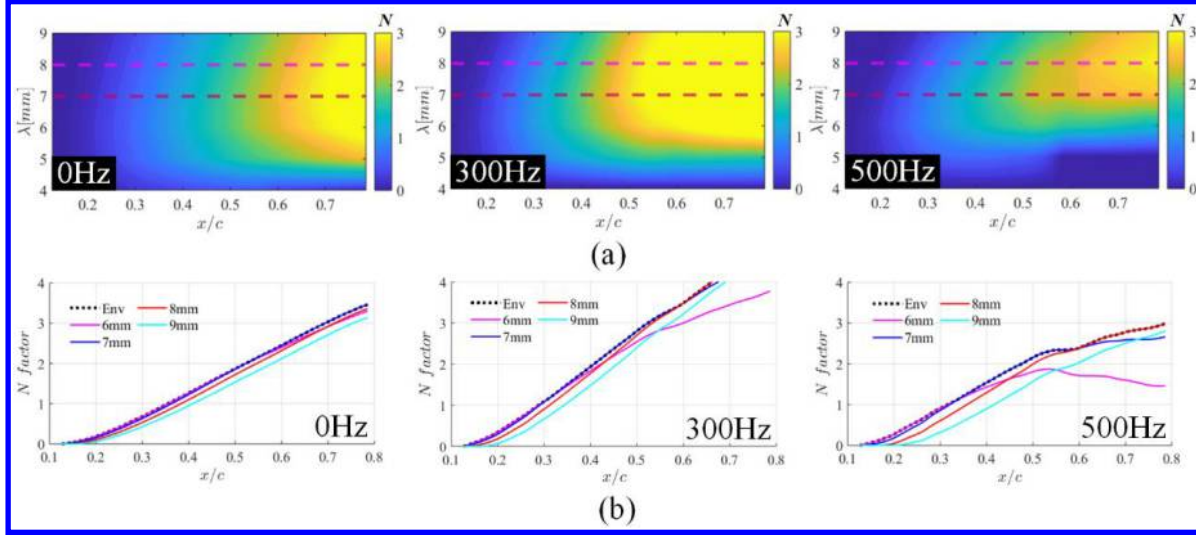

Fig. 8 (a) N-factor contours of stationary mode (0Hz) and traveling modes (300Hz and 500Hz). (b) Envolope N-factors of stationary mode (0Hz) and traveling modes (300Hz and 500Hz) along the x chord.

Fig.9 displays the envelope N-factors of various traveling modes from x/c_x=0.2 to 0.7. It evidently shows traveling modes from f=200Hz to 300Hz appear to be most amplified while higher frequency modes (above 800Hz) are depressed completely, which is in line with conclusions from [16] that lower frequency traveling modes are more unstable than higher frequency modes.
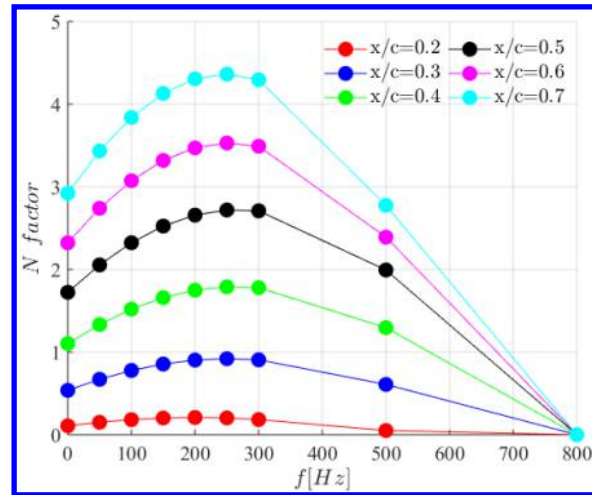

Fig. 9 Envolope N-factors of stationary mode (0Hz) and traveling modes (50Hz, 100Hz, 150Hz, 200Hz, 250Hz, 250Hz,300Hz, 500Hz and 800Hz) at various downstream locations

8

C. Infrared thermography

Following Reynolds analogy, flow with high shear convects heat faster compared with low shear flow [17]. Consequently, the technique of Infrared thermography has been extensively used for stationary CF vortices and the transition front detection where distinct shear flow regions are characterized. In this campaign, the spatial topology of primary stationary CF vortices are visualized by Infrared camera. For a better contrast as previously shown in [8], two halogen lamps are used to irradiate the wing model surface. In addition, the PET foil used as insert (as well as the PA dielectric material) is painted black. To avoid the interference caused by the roughness of black paint with the PA, the PET foil is only painted downstream of the PA location (as shown in fig.6).

The baseline case (without DRE and PA is off) is monitored with the freestream velocity of 22m/s (corresponding to Re_X approximately of 7.6×10^5) with α=3.5°. In this case, neither a stationary CF vortex nor a transition front is observed (not shown here), which suggests a broad laminar flow regime extension is achieved along the new model's pressure side. In fact, even with increasing Re_X number, the characterized jagged pattern usually indicating the transition front is still not observed in thermography images, suggesting stronger CF amplitude conditioning using DRE should be introduced. Therefore, a DRE array of one layer (100μm) is installed close to the leading edge (x/c_x=0.02) to enhance the stationary mode. The cylinder DRE array used here is fabricated with a spanwise-wavelength of 8mm (corresponding to the critical stationary mode from LST) featuring a diameter d=2mm. In the clean case (DRE installed and PA is off), however, still no distinct stationary CF vortex is observed except far downstream. Recalling the one layer DRE used here has been working efficiently on the reference model (*M3J*), the current weak vortices once again elucidate a mild CF growth in the new model's boundary layer (similar to the early stage of the *M3J*'s CF development).

After removing the previous one layer DRE, a second DRE array fabricated of 2 layers (height of 200μm) is installed close to the leading edge. As shown in fig.10, the flow is coming from the bottom (leading edge) to the top (trailing edge). It should be noted the dark region encompassing the PA is actually laminar flow. The lower temperature there is caused by the absence of black paint which means less heat is absorbed and emitted in that region compared with downstream. According to fig.10, uniform and outstanding stationary vortices are formed immediately after DRE as a result. This outcome coincides with results from pressure calculations in CFD simulation, where a relatively smooth pressure distribution growth and a small flow separation near the trailing edge are suggested. As an imitation of *M3J*'s C_p near the leading edge, CF instabilities develop in a consistent manner along the entire new model chord. In extra tuft visualizations (not shown), only a small separation is occurring near the trailing edge。
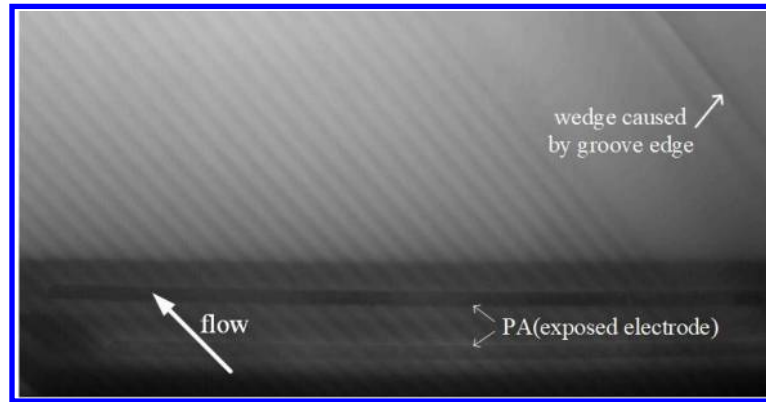

Fig. 10 IR image of the clean case (DRE with the height of 200μm)

The thermography results of the PA under various frequency actuation is presented in fig.11. In the current experiment, four AC modulation frequencies are tested with the same high voltage of 10kV peak-to-peak with the exception f_{AC}=5000Hz where 10kV was found excessively damaging the PA. The first row of images present results of testing cases where PA is actuated from f_{AC}=100Hz to 5000Hz whereas the second row is the corresponding subtractions with the clean case. Specifically, the black shadow in subtractions indicates the deformation of laminar flow because of introduced traveling modes. As shown in fig.11(a), the uniform stationary vortex pattern presented in the clean case becomes vague and shaded after turning on the PA, evidently demonstrating the ability of the PA to introduce traveling instabilities into the laminar boundary layer. When the PA is actuated under f_{AC}=100Hz, the stationary vortices are mildly deformed by the traveling modes while still retaining in the previous pattern as shown in fig.11(a). The moderate shadow presented in fig.11(b) illustrates the moderate effects of 100Hz mode as well. An evident change occurs in f_{AC}=250Hz and f_{AC}=500Hz cases. Both the raw image and subtraction suggest considerable

traveling modes contaminate the stationary mode and cause the boundary layer into full turbulence downstream of the PA strip. Increasing f_{AC} to higher value of $5000Hz$, the traveling mode contamination disappears and no visible flow change can be observed compared with the clean case. This outcome coincides at least qualitatively with LST prediction where traveling modes between $200Hz$ and $300Hz$ are suggested to be critical and higher frequency instabilities are supressed in spatial growth. As a result, the validity of LST for predicting and designing experiment aforehand is preliminarily confirmed.
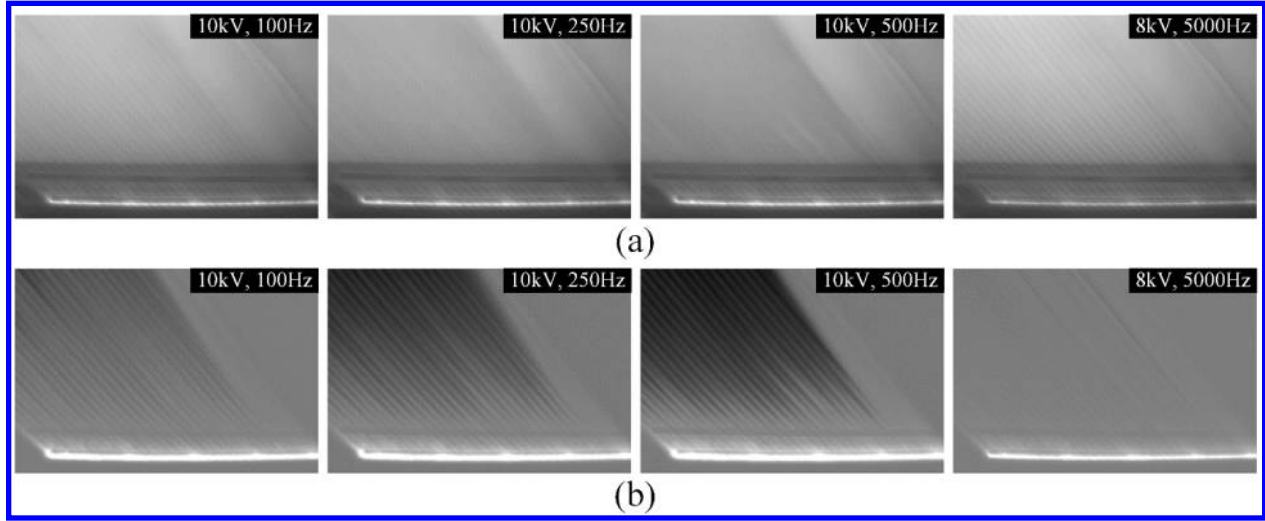

Fig. 11 (a) IR images with the PA working under 100Hz, 250Hz, 500Hz and 5000Hz.
(b) Corresponding IR image subtractions with the clean case.

D. PIV Measurement

In this section, the planar PIV measurement is implemented to give a quantitative view of the flow evolution as well as to validate conclusions from previous sections. Measuring is done at *y-z* plane at $x/c_x= 0.2$. As suggested in the thermography observation, the new model features a mild CF growth thus requiring stronger CF manipulation. In the following experiment, a DRE array of 2 layers (height of $200\mu m$) is chosen to induce stationary CF vortices and the PA supply power is adjusted appropriately in purpose of avoiding severely deforming stationary CF vortices. Considering the open-jet used for the current experiment features a turbulence intensity less than 0.04%, the contamination of uncontrolled perturbation (e.g. ambient turbulence and noise) is critically eliminated thus the unsteady modes are mainly caused by the PA actuation.

Results of time-average spanwise velocity (*w*) and its standard deviation (*w'*) at $x/c_x=0.2$ are present in fig.12. From the time-average velocity contour, five pronounced stationary vortices in total can be observed in the view domain (about 40mm wide), featuring a spanwise wavelength of 8mm which is a result of DRE forcing.

Moreover, the fact these stationary vortices are nearly equal-sized demonstrates the invariant spanwise conditioning, agreeing well with the pressure measurements (where the C_p upstream $x/c_x=0.4$ is almost identical between the two pressure tap arrays). All configurations in fig.12(a) clearly illustrate the primary stationary CF vortices remain nearly identical in different f_{AC} forcing, indicating the disturbances are introduced in a low amplitude by the PA. In the region of a single stationary CF vortex, temporal fluctuations are characterized mainly by 3 distinct types namely the type III (primary traveling CFI) as well as type I and type II (secondary CFI). In general, type III overlaps at the inner side of the upwelling vortex region and is a result from the interaction between stationary and traveling CFI [18]. The secondary instability type I and type II are located at the outer and upper side of the upwelling low momentum flow [19, 20] (i.e. the high shear region caused by primary stationary vortices) and their sudden growth are widely attributed to the final turbulence break down [7].
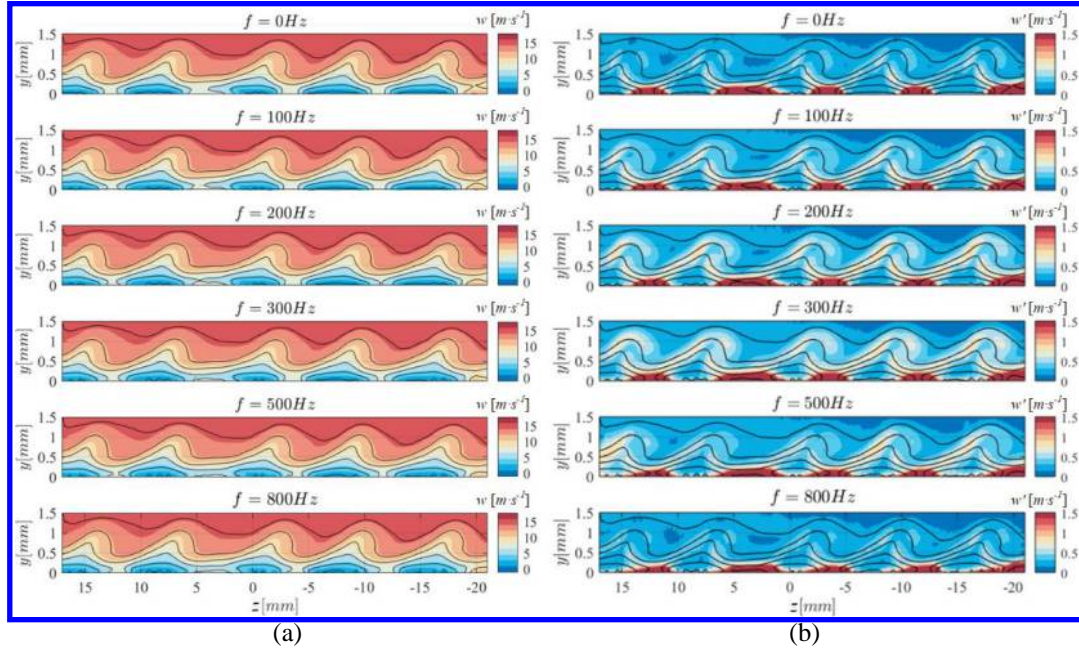
Fig. 12 (a) The average velocity *w* (seen from upstream) (b) The standard deviation *w'* (color scale) and the average velocity *w* (black lines)

Standard deviation contours shown in fig.12(b) clearly show the aforementioned three fluctuation types are observed as function of f_{AC} at the current chord location. This result is in line with the outcomes from the average velocity contour where the stationary vortices have formed in distinct shapes and approach to the characteristic lobe structure which is related to the onset of secondary CFI. However, it's surprising to find these strong type I and type II modes even in the clean case (0Hz). As mentioned before, secondary instabilities (type I & type II) are commonly thought to develop once primary CFI reaches saturation and their explosive spatial growths lead to transition immediately. Considering previous thermography results, no transition is observed under the condition of the 2-layer DRE array (200μm) in the measuring region (until x/c_x=0.8 where the pressure gradient becomes adverse). Therefore, the appearance of secondary CFI is not expected at the location which is far upstream (x/c_x =0.2).

According to the standard deviation contour of the clean case, type III mode has stronger amplitudes compared with type I and II, suggesting an interaction between stationary and traveling modes, thus primary CFI is in charge of boundary layer stability at current location. After switching on the PA and increasing f_{AC}, a considerable change takes place with respect to CFI. Within all the tested f_{AC}, it can be concluded that 200Hz and 300Hz are the most effective forcing as all the CFI types are evidently enhanced compared, which further coincides with LST and thermography results. Though f_{AC}=500 Hz shows great control effects on CFI as well, it should be reminded that PA is working at the same high voltage in all cases thus f_{AC}=500Hz forcing is inferred to have larger initial amplitudes than lower f_{AC} cases. In the contrary, no significant change of CFI is observed in f_{AC}=800Hz case even though the fluctuation receptivity in this case is supposed to be maximum. Recalling LST prediction, the boundary layer of the new model has a stabilizing effect on high frequency instabilities. As a result, instabilities induced by the PA (f_{AC}=800 Hz) are suppressed and fade away immediately.

V. Conclusion

In this paper, the procedure to design a new swept wing model which reproduces conditions of CFI receptivity and initial growth of a larger reference model (*M3J*) is presented in detail. First, a two-dimensional wing shape is designed by using *Xfoil* based on the initial C_p (near the leading edge) of the *M3J* model. Subsequently the performance of the new shape is verified by the RANS *k-ε* turbulence model in Comsol considering the windtunnel wall effects. The detailed design of the CAD model enables the new facility to include plasma actuator's effects on CFI. Consequently, the new model is verified by various measurement techniques including pressure measurement, Infrared thermography and PIV. The measured pressure distribution demonstrates spanwise-invariant conditions are achieved on this new model until 40% of the chord (*α*=3.5°). Based on the measured pressure distribution, the stability properties of the new model are predicted by LST. Consequently, the predicted critical stationary mode (*λ*=8*mm*) triggered by DRE is

11

visualized by Infrared thermography. Low frequency traveling modes (f=200Hz~300Hz) are observed to be most unstable both by Infrared thermography and PIV, in line with LST predictions. Finally, the appearance of three typical instability types (type I, type II and type III) occurs at x/c_x=0.2 in the clean case as these are strongly enhanced when the PA is actuated at low frequencies (f_{AC}=200Hz~500Hz). The experimental results validate the ability of this new swept wing model to study PA effects on the receptivity and initial growth of CFI.

Acknowledgments

References

[1]   Bippes, Hans. "Basic experiments on transition in three-dimensional boundary layers dominated by crossflow instability." Progress in aerospace sciences 35.4 (1999): 363-412.

[2]   Saric, William, and Helen Reed. "Crossflow instabilities-theory & technology." 41st Aerospace Sciences Meeting and Exhibit. 2003.

[3]   Enloe, C. L., et al. "Mechanisms and responses of a single dielectric barrier plasma actuator: plasma morphology." AIAA journal 42.3 (2004): 589-594.

[4]   Dörr, P. C., and M. J. Kloker. "Stabilisation of a three-dimensional boundary layer by base-flow manipulation using plasma actuators." Journal of Physics D: Applied Physics 48.28 (2015): 285205.

[5]   Dörr, P. C., and M. J. Kloker. "Transition control in a three-dimensional boundary layer by direct attenuation of nonlinear crossflow vortices using plasma actuators." International Journal of Heat and Fluid Flow 61 (2016): 449-465.

[6]   Dörr, Philipp C., and Markus J. Kloker. "Crossflow transition control by upstream flow deformation using plasma actuators." Journal of Applied Physics 121.6 (2017): 063303.

[7]   Serpieri, J. Crossflow Instability: Flow diagnostics and control of swept wing boundary layers. Diss. Delft University of Technology, 2018.

[8]   Yadala, Srikar, et al. "Experimental control of swept-wing transition through base-flow modification by plasma actuators." Journal of Fluid Mechanics 844 (2018).

[9]   Krishnan, K. S. G., O. Bertram, and O. Seibel. "Review of hybrid laminar flow control systems." Progress in Aerospace Sciences 93 (2017): 24-52.

[10]   Serpieri, Jacopo, and Marios Kotsonis. "Design of a swept wing wind tunnel model for study of crossflow instability." 33rd AIAA Applied Aerodynamics Conference. 2015.

[11]   Rius Vidales, Alberto F., et al. "Effect of Two-Dimensional Surface Irregularities on Swept Wing Transition: Forward Facing Steps." 2018 Fluid Dynamics Conference. 2018.

[12]   Merino-Martínez, Roberto, et al. "Aeroacoustic design and characterization of the 3D-printed, open-jet, anechoic wind tunnel of Delft University of Technology." Applied Acoustics 170 (2020): 107504.

[13]   Saric, William S., Andrew L. Carpenter, and Helen L. Reed. "Passive control of transition in three-dimensional boundary layers, with emphasis on discrete roughness elements." Philosophical Transactions of the Royal Society A: Mathematical, Physical and Engineering Sciences 369.1940 (2011): 1352-1364.

[14]   Guo, Zhengfei, and Markus J. Kloker. "Effects of Low-Frequency Noise in Crossflow Transition Control." AIAA Journal 58.3 (2020): 1068-1078.

[15]   Malik, Mujeeb R., et al. "Secondary instability of crossflow vortices and swept-wing boundary-layer transition." Journal of Fluid Mechanics 399 (1999): 85-115.

[16]   Guo, Zhengfei, and Markus J. Kloker. "Control of crossflow-vortex-induced transition by unsteady control vortices." Journal of Fluid Mechanics 871 (2019): 427-449.

[17]   Yadala Venkata, S., Hehner, M. T., Serpieri, J., Benard, N., & Kotsonis, M. (2018). Swept-wing transition control using DBD plasma actuators.

[18]   Janke, Erik, and Ponnampalam Balakumar. "On the secondary instability of three-dimensional boundary layers." Theoretical and Computational Fluid Dynamics 14.3 (2000): 167-194.

[19]   Wassermann, Peter, and Markus Kloker. "Transition mechanisms induced by travelling crossflow vortices in a three-dimensional boundary layer." Journal of Fluid Mechanics 483 (2003): 67.

[20]   Wassermann, Peter, and Markus Kloker. "Mechanisms and passive control of crossflow-vortex-induced transition in a three-dimensional boundary layer." Journal of Fluid Mechanics 456 (2002): 49.